

# Modeling Transmission Spectra in a Mach-Zehnder Interferometer

Ehsan<sup>1</sup>

<sup>1</sup>Department of Electrical and Computer Engineering, University of Alberta, 9211 116 Street,  
Edmonton, Alberta T6G 1H9, Canada  
[vahidzad@ualberta.ca](mailto:vahidzad@ualberta.ca)

**Abstract:** This study investigates the transmission characteristics of a Mach-Zehnder Interferometer (MZI) through simulation, focusing on the effects of varying key parameters such as arm lengths, and wavelength. The results reveal how these modifications influence the spectral output, providing insights into the MZI's performance and tunability.

## 1. Introduction

Photonic Integrated Circuits (PICs) have revolutionized the field of optics by enabling the miniaturization and integration of multiple optical components onto a single chip. These circuits play a crucial role in applications such as telecommunications, data processing, sensing, and quantum computing. Among the key components of PICs is the Mach-Zehnder Interferometer (MZI), a versatile device used for optical signal modulation, filtering, and switching. The MZI operates by splitting an input optical signal into two paths, introducing phase shifts through controlled variations in waveguide properties, and recombining the signals to produce interference. This allows precise control over the transmission spectrum, making MZIs indispensable for various wavelength-specific applications in integrated photonics.

## 2. Theory

A Mach-Zehnder Interferometer (MZI) shown in Figure 1, is a widely used device in optics and photonics for manipulating and analyzing light. It consists of two couplers (beam splitters) and two waveguides or arms. The input light is divided by the first coupler, propagates through the two arms, and is then recombined at the second coupler. The interference of the light at the output depends on the relative phase difference introduced between the two arms.

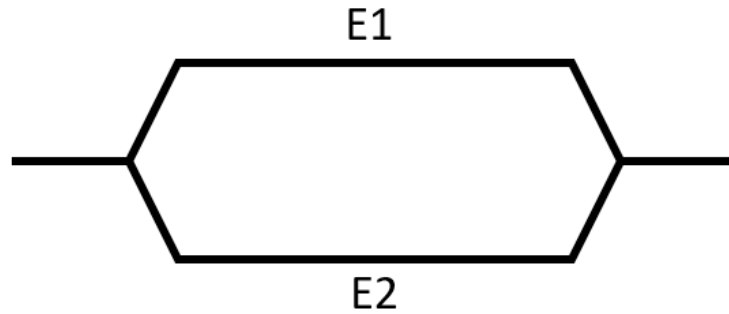


*Figure 1 Structure of a balanced MZI*

The electric field of light in an MZI can be represented mathematically to describe the interference. If the input field is  $E_0$ , the fields in the two arms are given by:

$$E_1 = \frac{E_0}{\sqrt{2}} e^{i\phi_1}, \quad E_2 = \frac{E_0}{\sqrt{2}} e^{i\phi_2}$$

where  $\phi_1$  and  $\phi_2$  are the phase shifts in the two arms. The phase shift is a function of the effective refractive index  $n_{\text{eff}}$ , arm length  $L$ , and wavelength  $\lambda$ :

$$\phi = \frac{2\pi n_{\text{eff}} L}{\lambda}.$$

The recombined field at the output is the superposition of the two fields:

$$E_{\text{out}} = E_1 + E_2 = \frac{E_0}{\sqrt{2}} (e^{i\phi_1} + e^{i\phi_2}).$$

The resulting intensity is proportional to the square of the output field magnitude:

$$I_{\text{out}} \propto |E_{\text{out}}|^2 = \frac{I_0}{2} [1 + \cos(\Delta\phi)],$$

where  $\Delta\phi = \phi_2 - \phi_1$  is the relative phase difference.

The Free Spectral Range (FSR) is the wavelength spacing between consecutive constructive or destructive interference peaks in the MZI's transmission spectrum. It is determined by the optical path length difference  $\Delta L$  between the two arms:

$$\text{FSR} = \frac{\lambda^2}{n_{\text{eff}} \Delta L}.$$

### 3. Simulation

#### 3.1 Lumerical Mode

A waveguide structure based on silicon-on-insulator (SOI) technology was simulated to calculate the fundamental transverse electric (TE) mode. The waveguide comprises a silicon core with a thickness of 220 nm, positioned atop a silicon dioxide (SiO<sub>2</sub>) substrate, which serves as the cladding. The waveguide width was specified as 500 nm, a standard dimension for ensuring single-mode operation at telecommunication wavelengths around 1550 nm. The SOI platform was chosen due to its high refractive index contrast between the silicon core ( $n \sim 3.48$  at 1550 nm) and the silicon dioxide cladding ( $n \sim 1.44$ ), which provides strong optical confinement and supports compact photonic device designs.

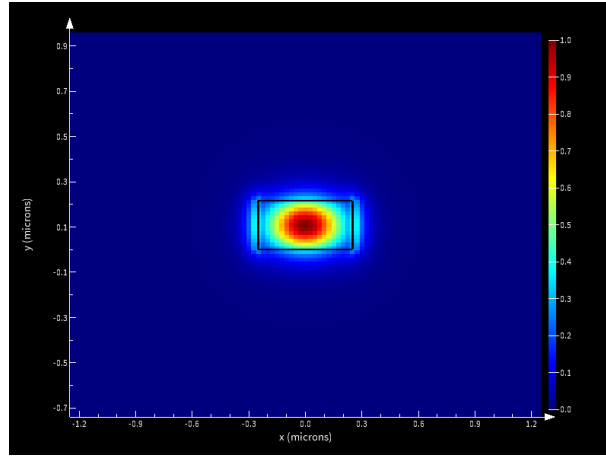


Figure 2 Mode profiles fundamental TE of a waveguide with width = and thickness = 220.

The effective index and group index of fundamental TE mode at wavelength range of 1500-1600 nm is shown in Figure 2 and Figure 3, respectively.

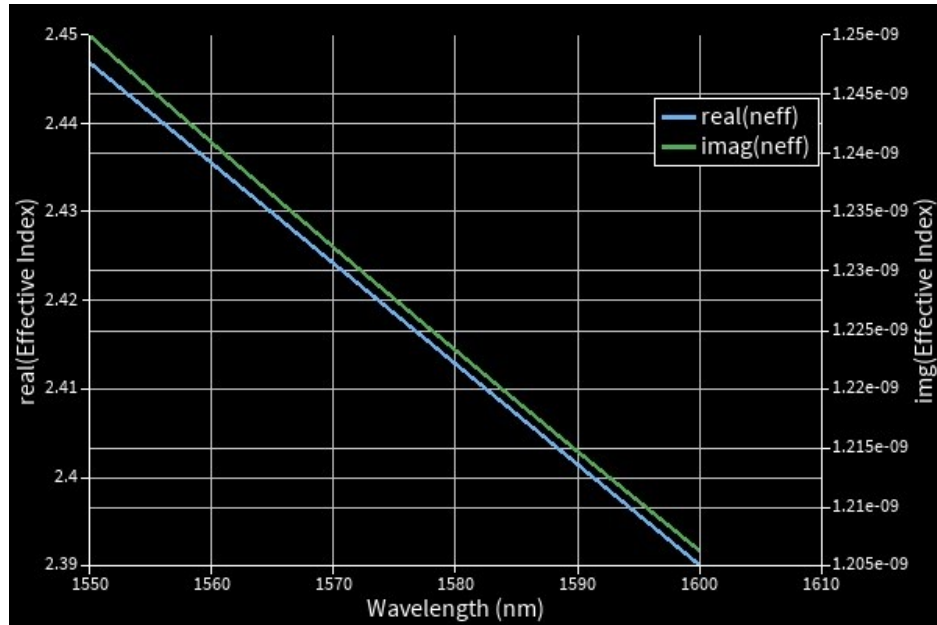


Figure 3 real and imaginary parts of effective index for the fundamental TE mode of the waveguide

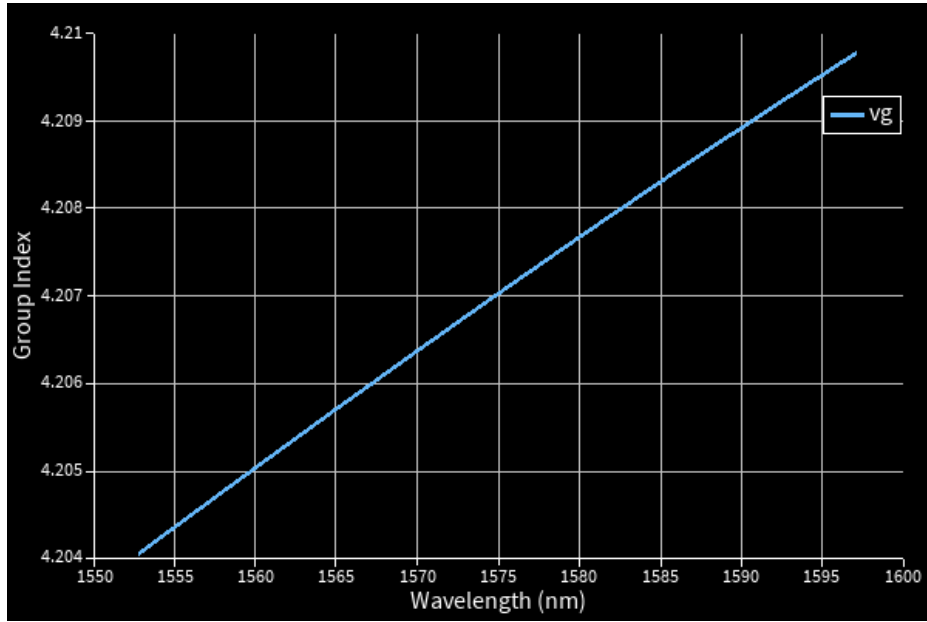


Figure 4 group index of the waveguide as a function of wavelength

To describe the wavelength dependence of the  $n_{\text{eff}}$ , Taylor expansion is utilized to develop a compact model for the waveguide based on the following formula:

$$n_{\text{eff}}(\lambda) = 2.44 + 1.13.(\lambda - 1.55) - 0.044.(\lambda - 1.55)^2$$

### 3.2 Lumerical Interconnect

Lumerical interconnect was utilized to measure the transmission spectrum of different unbalanced MZIs. The two arms were designed with different optical path lengths ( $\Delta L$ ). This parameter,  $\Delta L$ , directly influences the phase difference between the arms and, consequently, the interference pattern observed in the output spectrum. To analyze the impact of varying  $\Delta L$  on the MZI's transmission characteristics, multiple configurations were simulated with different arm length differences. Examples include MZIs with  $\Delta L=50 \mu\text{m}$  and  $\Delta L=100 \mu\text{m}$  shown in figure 4. These specific values demonstrate how changes in  $\Delta L$  affect the FSR and the spectral resolution of the device.

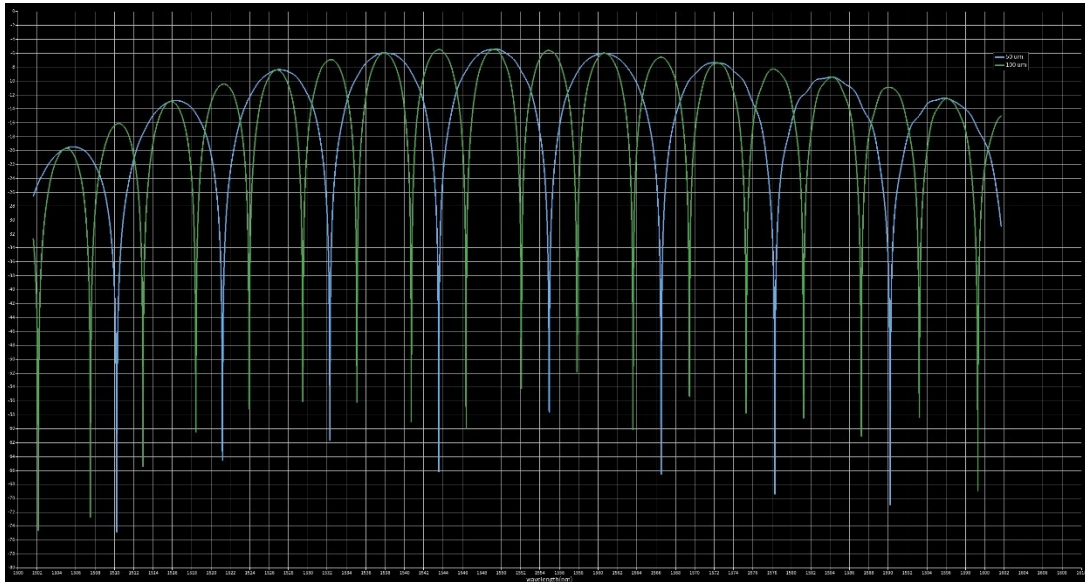


Figure 5 the transmission spectra of two unbalanced MZIs with  $\Delta L=50$  (Blue) and  $\Delta L=100$  (Green)

### 3.3 Layout

KLayout and SiEPIC toolkit were utilized to design the layout of five different Mach-Zehnder Interferometers (MZIs), each with varying path length differences ( $\Delta L$ ). The  $\Delta L$  values ranged from 25  $\mu\text{m}$  to 200  $\mu\text{m}$ , allowing for the investigation of the impact of optical path length variation on interference patterns. The layouts of these MZIs are shown in figure 5. The  $\Delta L$  for the Mach-Zehnder Interferometers (MZI1 to MZI5) follows an incremental pattern, with  $\Delta L$  set to 25  $\mu\text{m}$ , 50  $\mu\text{m}$ , 100  $\mu\text{m}$ , 150  $\mu\text{m}$ , and 200  $\mu\text{m}$  for MZI1, MZI2, MZI3, MZI4, and MZI5, respectively.

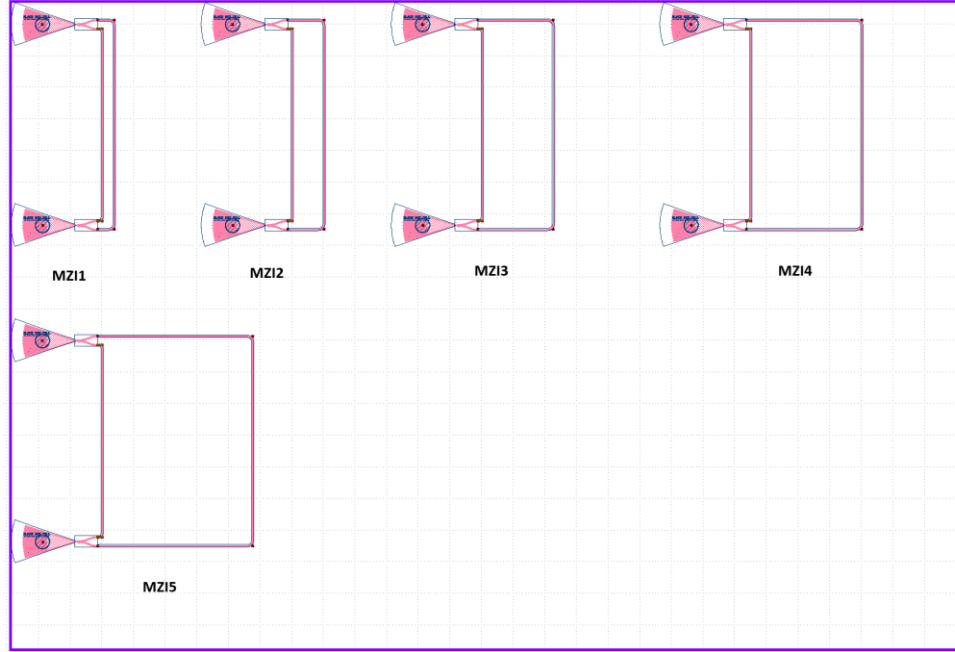


Figure 6 - Submitted layout for fabrication containing 5 different MZI

### 3.4 Manufacturing Challenges

To account for manufacturing variability, a corner analysis was performed considering a nominal waveguide width of 500 nm and a nominal thickness of 220 nm. The wafer thickness was assumed to vary within a range of 215.3 nm to 223.1 nm, while the waveguide width was varied between 470 nm and 510 nm. A total of five different simulations were conducted to evaluate the impact of these variations on device performance.

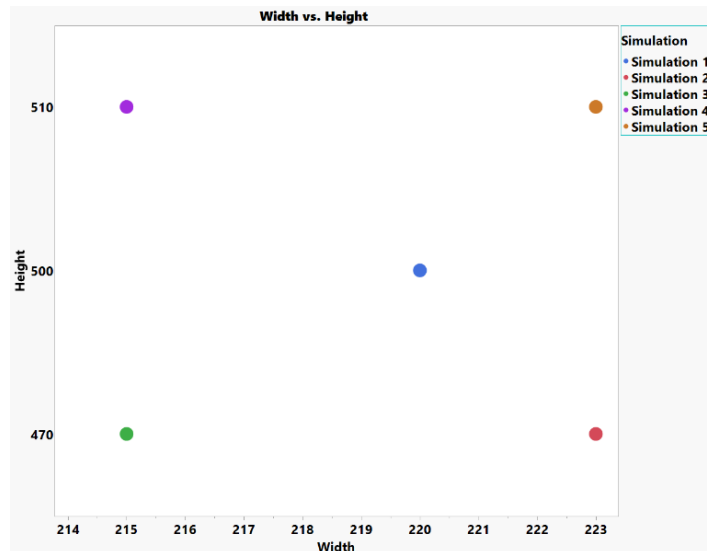


Figure 7 – Simulation grid used for corner analysis

Figure 8 presents the results of the corner analysis, illustrating the variations in both the group index ( $n_g$ ) and the effective index across the five different simulation cases. This analysis accounts for manufacturing-induced deviations in waveguide width and wafer thickness. As observed from the simulation results, the group index exhibits a variation within the range of approximately 4.17 to 4.26, while the effective index fluctuates between 2.37 and 2.47. These variations arise due to fabrication tolerances, which influence the waveguide geometry and, consequently, the optical mode confinement and propagation characteristics.

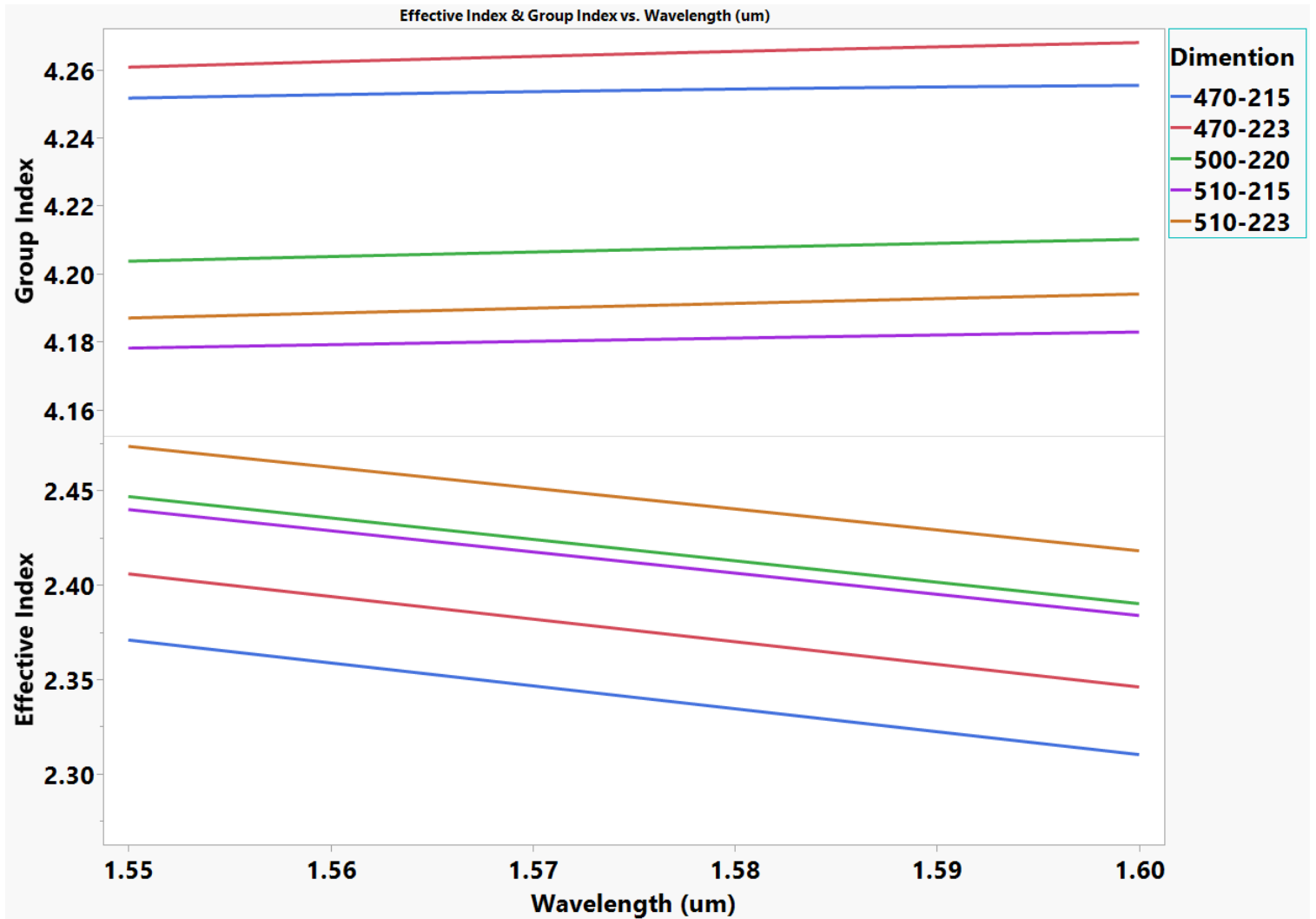


Figure 8 - Corner analysis for different dimensions of waveguides

#### 4. Summary of the fabrication Description

The photonic devices were fabricated using the NanoSOI MPW fabrication process by Applied Nanotools Inc. (<http://www.appliednt.com/nanosoi>; Edmonton, Canada) which is based on direct-write 100 keV electron beam lithography technology. Silicon-on-insulator wafers of 200 mm diameter, 220 nm device thickness and 2  $\mu\text{m}$  buffer oxide thickness are used as the base material for the fabrication. The wafer was pre-diced into square substrates with dimensions of 25x25 mm, and lines were scribed into the substrate backsides to facilitate easy separation into smaller chips once fabrication was complete. After an initial wafer clean using piranha solution (3:1  $\text{H}_2\text{SO}_4\text{:H}_2\text{O}_2$ ) for 15 minutes and water/IPA rinse, hydrogen silsesquioxane (HSQ) resist was spin-coated onto the substrate and heated to evaporate the solvent. The photonic devices were patterned using a JEOL JBX-8100FS electron beam instrument at The University of British Columbia. The exposure dosage of the design was corrected for proximity effects that result from the backscatter of electrons from exposure of nearby features. Shape writing order was optimized for efficient patterning and minimal beam drift. After the e-beam exposure and subsequent development with a tetramethylammonium sulfate (TMAH) solution, the devices were inspected optically for residues and/or defects. The chips were then mounted on a 4" handle wafer and underwent an anisotropic ICP-RIE etch process using chlorine after qualification of the etch rate. The resist was removed from the surface of the devices using a 10:1 buffer oxide wet etch, and the devices were inspected using a scanning electron microscope (SEM) to verify patterning and etch quality. A 2.2  $\mu\text{m}$  oxide cladding was deposited using a plasma-enhanced chemical vapour deposition (PECVD) process based on tetraethyl orthosilicate (TEOS) at 300°C. Reflectometry measurements were performed throughout the process to verify the device layer, buffer oxide and cladding thicknesses before delivery.

#### 5. Measurement description

To characterize the devices, a custom-built automated test setup [1, 2] with automated control software written in Python was used [3]. An Agilent 81600B tunable laser was used as the input source and Agilent 81635A optical power sensors as the output detectors. The wavelength was swept from 1500 to 1600 nm in 10 pm steps. A polarization maintaining (PM) fibre was used to maintain the polarization state of the light, to couple the TE polarization into the grating couplers [4]. A 90° rotation was used to inject light into the TM grating couplers [4]. A polarization maintaining fibre array was used to couple light in/out of the chip [5].

#### 6. Measurements

To accurately assess the performance of the designed devices, key waveguide parameters were extracted from experimental measurements. One of the most critical parameters evaluated was the group index ( $n_g$ ) of the waveguides. To achieve precise determination of  $n_g$  and the free spectral range (FSR) of the MZIs, an advanced curve-fitting technique, known as autocorrelation fitting, was employed. This method enables a robust and reliable estimation by minimizing discrepancies between measured transmission spectra and theoretical predictions.

For each experimental measurement, the autocorrelation fitting process was applied to extract the best-fit values for the  $n_g$  and FSR. These values were determined based on the fitted spectral data, providing an accurate representation of the waveguide dispersion characteristics. Figure 9 illustrates a comparison between the measured transmission spectra and the fitted results for MZI1 through MZI5, highlighting the effectiveness of the applied curve-fitting approach in modeling the optical behavior of the fabricated devices. Furthermore, the measured  $n_g$  values and the corresponding FSR for each MZI are reported in Table 1. These extracted values confirm that the fabricated devices exhibit strong agreement with theoretical simulations and calculations, validating the accuracy of the fabrication process and the reliability of the design methodology.

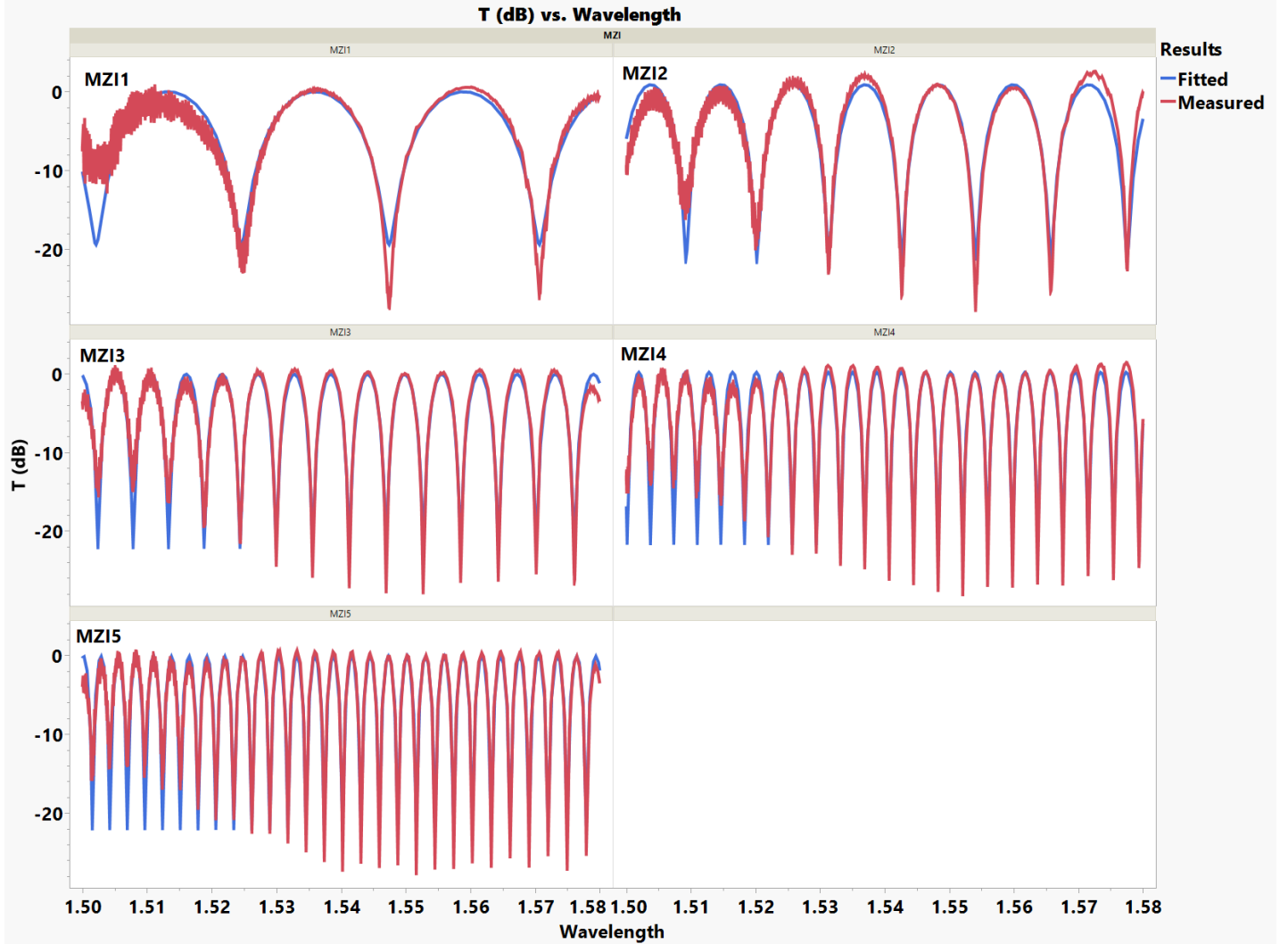


Figure 9 - Measured transmission spectrum of MZIs (Red) and fitted transmission spectrum of MZIs (Blue).



*Table 1 – Summary of calculated, simulated, and measured properties of fabricated MZIs*

Delta L (nm)	Calculated FSR	Simulated FSR	Calculated FSR Based on Measurements	Calculated $n_g$ Based on Measurements
25	22.8	21	23	4.26
50	11.4	11.1	11.4	4.17
100	5.7	5.7	5.7	4.18
150	3.8	3.8	3.8	4.18
200	2.8	2.8	2.85	4.18

## 7. Acknowledgment

I acknowledge the edX UBCx Phot1x Silicon Photonics Design, Fabrication and Data Analysis course, which is supported by the Natural Sciences and Engineering Research Council of Canada (NSERC) Silicon Electronic-Photonic Integrated Circuits (SiEPIC) Program. The devices were fabricated by Richard Bojko at the University of Washington Washington Nanofabrication Facility, part of the National Science Foundation's National Nanotechnology Infrastructure Network (NNIN), and Cameron Horvath at Applied Nanotools, Inc. Omid Esmaeeli performed the measurements at The University of British Columbia. We acknowledge Lumerical Solutions, Inc., Mathworks, Mentor Graphics, Python, and KLayout for the design software.

## 7. References

- [1] Lukas Chrostowski, Michael Hochberg, chapter 12 in "Silicon Photonics Design: From Devices to Systems", Cambridge University Press, 2015
- [2] <http://mapleleafphotonics.com>, Maple Leaf Photonics, Seattle WA, USA.
- [3] <http://siepic.ubc.ca/probestation>, using Python code developed by Michael Caverley.
- [4] Yun Wang, Xu Wang, Jonas Flueckiger, Han Yun, Wei Shi, Richard Bojko, Nicolas A. F. Jaeger, Lukas Chrostowski, "Focusing sub-wavelength grating couplers with low back reflections for rapid prototyping of silicon photonic circuits", Optics Express Vol. 22, Issue 17, pp. 20652-20662 (2014) doi: 10.1364/OE.22.020652
- [5] [www.plcconnections.com](http://www.plcconnections.com), PLC Connections, Columbus OH, USA.